Atomic momentum distribution and Bose-Einstein condensation in liquid ^{4}He under pressure

H. R. Glyde,[1] S. O. Diallo,[2] R. T. Azuah,[3,4] O. Kirichek,[5] and J. W. Taylor[5]

[1]*Department of Physics and Astronomy, University of Delaware, Newark, Delaware 19716-2593, USA*

[2]*Spallation Neutron Source, Oak Ridge National Laboratory, Oak Ridge, Tennessee 37831, USA*

[3]*NIST Center for Neutron Research, Gaithersburg, Maryland 20899-8562, USA*

[4]*Department of Materials Science and Engineering, University of Maryland, College Park, Maryland 20742-2115, USA*

[5]*ISIS Spallation Neutron Source, STFC, Rutherford Appleton Laboratory, Didcot OX11 0QX, United Kingdom*

(Received 30 August 2011; revised manuscript received 8 October 2011; published 7 November 2011)

Neutron-scattering measurements of the dynamic structure factor, $S(Q,\omega)$, of liquid ^{4}He as a function of pressure at high-momentum transfer, $\hbar Q$, are presented. At high $\hbar Q$ the dynamics of single atoms in the liquid is observed. From $S(Q,\omega)$ the atomic momentum distribution, $n(\mathbf{k})$, the Bose-Einstein condensate fraction, n_0, and the final-state (FS) broadening function are obtained. The shape of $n(\mathbf{k})$ differs from a classical, Maxwell-Boltzmann distribution with higher occupation of low-momentum states in the quantum liquid. The width of $n(\mathbf{k})$ and the atomic kinetic energy, $\langle K\rangle$, increase with pressure but the shape of $n(\mathbf{k})$ remains approximately independent of pressure. The present observed and Monte Carlo (MC) calculations of $\langle K\rangle$ agree within error. The condensate fraction decreases from $n_0 = 7.25\% \pm 0.75\%$ at saturated vapor pressure ($p \simeq 0$) to $n_0 = 3.2\% \pm 0.75\%$ at pressure $p = 24$ bar, a density dependence that is again reproduced by MC calculations within observed error. The FS function is the contribution to $S(Q,\omega)$ arising from the interaction of the struck atom with its neighbors following the scattering. The FS function broadens with increasing pressure reflecting the increased importance of FS effects at higher pressure.

DOI: 10.1103/PhysRevB.84.184506 PACS number(s): 61.05.fg, 67.10.Ba

I. INTRODUCTION

Bose-Einstein condensation (BEC) plays an essential role and is widely observed in condensed matter.[1] Superfluidity and superconductivity arise from BEC.[2–5] Superfluidity in liquid ^{4}He is a manifestation of BEC of preformed bosons (^{4}He atoms).[6,7] Superconductivity follows from BEC of paired fermions (Cooper pairs) and is generally limited by the formation of the pairs. In dilute gases of trapped Bose alkali atoms, essentially 100% of the atoms can Bose condense. BEC in a gas of photons, in which the number photons is restricted, has also recently been reported.[8]

BEC may be described as the condensation of a macroscopic fraction of the Bosons into one single-particle state, usually the lowest-energy single-particle state or ground-state orbital.[5] For bosons in a trap, the wave functions of the natural single-particle orbitals are determined chiefly by the trapping potential and less so by the interparticle interaction. The natural orbitals are most fundamentally determined by diagonalizing the one-body density matrix (OBDM).[5,9–11] BEC is detected by the localization of the atoms in space when the atoms condense into the lowest energy orbital.[12–14]

In a uniform liquid where there is no external potential, the natural single-particle states are plane wave states enumerated by the single particle momentum, k. In this case BEC is associated with condensation into the zero-momentum ($k = 0$) state. In a uniform system, BEC can be observed as the onset of a peak in the momentum distribution, $n(\mathbf{k})$, at $k = 0$ of magnitude $n_0\delta(k)$, where n_0 is the condensate fraction. In this case, the OBDM is the Fourier transform of $n(\mathbf{k})$. In strongly interacting liquid ^{4}He fewer than 10% of atoms can condense. Nonetheless, the resulting phase coherence in the liquid enables superflow and other remarkable properties.

The atomic momentum distribution, $n^*(\mathbf{k})$, of atoms in the states $k > 0$ above the condensate in quantum gases, liquids, and solids is also of great interest. In classical systems where the momentum and position are independent variables, $n^*(\mathbf{k})$ is always a Gaussian function, the Maxwell-Boltzmann distribution. In quantum systems where the momentum and position are coupled via commutation relations, $n^*(\mathbf{k})$ depends on the interatomic potential, on the external potential, if any, and contains important information on quantum effects and interatomic correlations. In strongly interacting systems, $n^*(\mathbf{k})$ is a dominant part of $n(\mathbf{k})$.

As proposed initially by Miller, Pines, and Nozières[15] and Hohenberg and Platzman,[16] $n(\mathbf{k})$ and n_0 can be measured in neutron scattering measurements of the dynamic structure factor (DSF), $S(Q,\omega)$. At high-energy ($\hbar\omega$) and -momentum ($\hbar Q$) transfer from the neutron to the liquid, the neutron strikes a single atom and $S(Q,\omega)$ is a broad function of ω centered near the free-atom recoil frequency $\omega_R = \hbar Q^2/2m$ of width proportional to $v_R = \hbar Q/m$, the free atom recoil velocity. In this momentum and energy transfer range, it is convenient to express the energy transfer ω terms of the y scaling variable $y = (\omega - \omega_R)/v_R$ and introduce the DSF $J(Q,y) = v_R S(Q,\omega)$. The scattering is then centered near $y = 0$ and the width is approximately independent of Q. If the interaction of the struck atom with its neighbors following the scattering can be ignored, denoted the impulse approximation (IA), the $J(Q,y)$ reduces to $J_{\rm IA}(y)$, which is entirely independent of Q. The condensate appears in $J_{\rm IA}(y)$ as a term $n_0\delta(y)$ and $J_{\rm IA}(y)$ has a width arising from Doppler broadening by the atomic momentum distribution, $n(\mathbf{k})$.

When there is interaction, the atoms struck by neutrons collide with their neighbors following the scattering, denoted final-state (FS) interactions. When FS effects are important, the condensate is observed in $J(Q,y)$ at $y = 0$ as a broadened peak of width $n_0R(Q,y)$, where $R(Q,y)$ is the FS function. It is also observed in $J(Q,y)$ at $y \neq 0$ as a function that tracks

$R(Q,y)$. Because of FS effects, the observed $J(Q,y)$ also depends on Q. This dependence can be used to determine the FS function. In the absence of FS effects $R(Q,y) \rightarrow \delta(y)$.

Early measurements of the atomic momentum distribution and $n_0(T)$ in liquid ^{4}He using neutron inelastic scattering are reviewed by Sokol,[17] Glyde,[18] Silver and Sokol,[19] Glyde and Svensson,[20] Svensson and Sears,[21] Svensson,[22] and others. They produced a wide range of n_0 values,[23] $2\% \leqslant n_0 \leqslant 17\%$. The different values of n_0 arose chiefly from the different treatment of the FS contributions to $S(Q,\omega)$. Sears *et al.*[24] developed a method for treating FS effects based on an additive expansion[25] of $S(Q,\omega)$. Using this method and reactor neutron measurements of $S(Q,\omega)$ at wave vectors $10 \leqslant Q \leqslant 13$ Å^{-1}, Sears *et al.*[24] and Mook[26] obtained the first consistent values of n_0, $n_0(0) = 13.9\% \pm 2.3\%$ and $n_0(0) = 11\% \pm 3\%$, respectively. In an important step forward, Sokol and collaborators[17,27–31] made a series of measurements at higher Q values ($Q = 23$ Å^{-1}) drawing on the Intense Pulsed Neutron Source spallation neutron source. They also analyzed the data using the convolution method of treating FS effects developed by Gersch and Rodriguez[32] and the FS function calculated by Silver and Sokol.[19,33] They found $n_0 = 10.0\% \pm 1.25\%$ at low temperature (0.35 K) in liquid ^{4}He at saturated vapor pressure (SVP) and an n_0 that decreased significantly with increasing pressure, to $n_0 = 5.5\% \pm 1.25\%$ at 24 bar.

Taking advantage of the increased neutron beam intensity and improved instrumentation at the ISIS Spallation Neutron Source, Rutherford Appleton Laboratory, we have measured n_0 with increased precision. A condensate fraction at SVP of $n_0 = 7.25\% \pm 0.75\%$ was observed.[34] Similarly in ^{3}He-^{4}He mixtures, again at SVP, an n_0 that increases only slightly with ^{3}He concentration, to $n_0 = 11.0\% \pm 3.0\%$ at a ^{3}He concentration of 15%–20% was also observed.[35] The treatment of FS effects in these and the present measurements may be described as an expansion of $J(Q,y)$ at short scattering times in the spirit proposed by Sears[25] but within the convolution formulation of Gersch and Rodriguez.[32] The FS broadening function is also determined from experiment. These measurements[34–36] also showed that $n(\mathbf{k})$ in liquid helium is more sharply peaked at low k than a Gaussian. This deviation from a Gaussian can be described by a kurtosis of $\delta = 0.4$. A number of measurements of the atomic kinetic energy in liquid ^{4}He have been made at much higher Q ($Q \geqslant 100$ Å^{-1}), where FS effects are negligible, using the VESUVIO instrument at ISIS. These measurements and a wide range of measurements in other systems made using VESUVIO are reviewed by Andreani *et al.*[37]

In this background we present neutron-scattering measurements of $J(Q,y)$ in liquid helium under pressure between SVP and 24 bar at ISIS. The goal is to determine the condensate fraction, n_0, up to 24 bar to the same level of precision that it is known at SVP. We are particularly interested in how much the condensate fraction, n_0, decreases with increasing pressure between SVP ($p \simeq 0$) and the solidification pressure ($p = 25.3$ bar). A second goal is to determine the shape and width of $n^*(\mathbf{k})$ and whether this shape changes with pressure. The FS function is also determined as a function of pressure from experiment. A short version of this work has already appeared.[38]

In the next section we describe the model OBDM, DSF, and FS function $R(Q,s)$ used to analyze data and the experiment. In Sec. III we present the results and discuss them in Sec. IV.

II. EXPERIMENT AND DATA ANALYSIS

A. Model momentum distribution and OBDM

To represent $n(\mathbf{k})$, we introduce the model momentum distribution,[24,39]

$$n(\mathbf{k}) = n_0[\delta(\mathbf{k}) + f(\mathbf{k})] + A_1 n^*(\mathbf{k}). \quad (1)$$

In fundamental treatments of Bose fluids the occupation operators (a_k) are separated into a condensate component ($a_0 = \sqrt{n_0}$) and an above-the-condensate component ($a_k, k \neq 0$). This leads to the separation of $n(\mathbf{k})$ into $n_0\delta(\mathbf{k})$ and $n^*(\mathbf{k})$ in Eq. (1) the condensate and the above-the-condensate components, respectively. In interacting Bose fluids there is also a coupling between these components represented by the term

$$n_0 f(\mathbf{k}) = \left[\frac{n_0 mc}{2\hbar(2\pi)^3 n}\frac{1}{|\mathbf{k}|}\coth\left(\frac{c\hbar|\mathbf{k}|}{2k_B T}\right)\right] e^{-k^2/(2k_c^2)}, \quad (2)$$

where m is the mass, c is the sound velocity, and $n = N/V$ is the number density. This coupling arises from the scattering of bosons from states above the condensate into the condensate and vice versa. The scattering couples the single-particle [$n(\mathbf{k})$] and density (phonon-roton) excitations. It is the coupling of these excitations that leads to Eq. (2), which is derived and valid for low-k modes where it is most important. The coupling decreases at higher k values ($k \geqslant 0.7$ Å). We have multiplied the derived $f(\mathbf{k})$ by a Gaussian function $\exp[-k^2/(2k_c^2)]$ with $k_c = 0.5$ Å to cut off $f(\mathbf{k})$ in a smooth fashion at higher k as required. Eq. (2) is derived and discussed in Ref. 18. It is a small term and including it in Eq. (1) reduces the n_0 observed by approximately 15%.

The Fourier transform of $n(\mathbf{k})$ is the OBDM,

$$n(\mathbf{r}) = \langle\Psi^+(r)\Psi(\mathbf{0})\rangle/n = \langle e^{-i\mathbf{k}\cdot\mathbf{r}}\rangle = \int d\mathbf{k}\, n(\mathbf{k}) e^{-i\mathbf{k}\cdot\mathbf{r}}. \quad (3)$$

The OBDM is a more fundamental quantity than $n(\mathbf{k})$ since it is well defined for both strongly interacting and noninteracting systems. It represents the probability amplitude of simultaneously removing a particle from the origin and placing it at point $\mathbf{r}$. It is independent of the basis of the system. The model OBDM corresponding to Eq. (1), the Fourier transform of Eq. (1) for displacements $\mathbf{r} = \widehat{\mathbf{Q}}\, s$ parallel to the scattering wave vector, $\mathbf{Q}$, is

$$n(s) = n_0[1 + f(s)] + A_1 n^*(s). \quad (4)$$

The constant A_1 is determined by normalizing $n(\mathbf{k})$ to unity, that is, requiring $n(s = 0) = 1$. At $s = 0$, $f(0) = 0.28$. We begin with $n(s)$ in Eq. (4) as our basic model function that will be fitted to the data.

B. Observed dynamic structure factor

In this section, we set out the expressions for the DSF that we use to fit to the data. In inelastic neutron scattering from pure liquid ^{4}He, the coherent DSF, $S(Q,\omega)$, is always observed.

The coherent $S(Q,\omega)$ includes the dynamic correlations between atoms in the fluid. However, at high-momentum transfer $Q \geqslant$ 10–12 Å^{-1}, where the static structure factor, $S(Q)$, reduces to one, the correlations have little impact and the coherent $S(Q,\omega)$ reduces to the incoherent DSF, $S_i(Q,\omega)$. The $S_i(Q,\omega)$ describes the response of the single atom that is struck by the neutron. As discussed in the Introduction, at large, constant Q, $S_i(Q,\omega)$ is a broad function of ω peaked at approximately at ω_R of width proportional to v_R and magnitude inversely proportional to v_R. In this regime, the near impulse regime, it is convenient to express the energy transfer in terms of the y-scaling variable and $S_i(Q,\omega)$ as $J(Q,y) = v_R S(Q,\omega)$. The $J(Q,y)$ peaks near $y = 0$ and is approximately independent of Q.

The Fourier transform of $S_i(Q,\omega)$, the intermediate DSF $S_i(Q,t)$, is similarly conveniently expressed in terms of the length $s = v_R t$ conjugate to y. In these variables, the Fourier transform of $J(Q,y)$ is

$$J(Q,y) = \frac{1}{2\pi}\int ds\, e^{iys} J(Q,s), \tag{5}$$

where $J(Q,s)$ is the intermediate DSF written in the length variable, s.

The intermediate DSF in the IA is also exactly the OBDM,

$$J_{\rm IA}(s) = n(s) = n_0[1 + f(s)] + A_1 n^*(s). \tag{6}$$

This equality also makes $n(s)$ a natural function to fit to the data. The observed intermediate DSF is

$$J(Q,s) = J_{\rm IA}(s) R(Q,s), \tag{7}$$

where $R(Q,s)$ is the FS broadening function that takes account of the interaction of the struck atom with its neighbors. Equation (7) can be taken as the definition of the FS function. As discussed below we obtain functions for both $n^*(s)$ and $R(Q,s)$ by making an expansion of $J(Q,s)$ in powers of s that is qualitatively correct up to s^6 and determine the parameters in the expansion by fits to experiment. In this way $R(Q,s)$ is determined experimentally and is a function of pressure.

At high wave vector and energy transfer, the scattering time is short. The recoil distance $s = v_R t$ traveled by the struck atom within the scattering time is also short. For short s the intermediate DSF in Eq. (7) can be written as

$$J(Q,s) = \left\langle T_s \exp\left[-i\int_0^s ds' k_Q(s')\right]\right\rangle. \tag{8}$$

In this expression $T_s(T_t)$ is the distance (time) ordering operator and $\hbar k_Q = \hbar(\mathbf{k}\cdot\hat{\mathbf{Q}})$ is the momentum of the struck atom along $\mathbf{Q}$. From Eq. (8) we see that $J(Q,s)$ depends only on the momentum of the struck atom, the initial momentum $k_Q(0)$ and the momentum after it has traveled a distance s away from the scattering event. The $k_Q(s)$ differs from $k_Q(0)$ as a result of collisions of the recoiling struck atom with its neighbors, the FS effects. If we ignore these FS collisions so that $k_Q(s) = k_Q(0)$ for all s, $J(Q,s)$ reduces to the IA,

$$J_{\rm IA}(s) = \langle e^{-ik_Q s}\rangle. \tag{9}$$

The IA assumes that the momentum k_Q of the struck atom is constant and not changed from its initial value after the scattering (no FS interactions). By comparing Eqs. (3) and (9) we see that the intermediate DSF in the IA is the OBDM for displacements $\mathbf{r} = \hat{\mathbf{Q}}s$ parallel to $\mathbf{Q}$.

To obtain the expressions for $J_{\rm IA}(s)$ and the FS function $R(Q,y)$ that we fit to data, we make cumulant expansions of Eqs. (8) and (9). The cumulant expansion of the OBDM Eq. (9) gives, up to terms in s^6,

$$J^*_{\rm IA}(s) = n^*(s) = \exp\left[-\frac{\overline{\alpha}_2 s^2}{2!} + \frac{\overline{\alpha}_4 s^4}{4!} - \frac{\overline{\alpha}_6 s^6}{6!}\right], \tag{10}$$

where

$$\begin{aligned} \overline{\alpha}_2 &= \langle k_Q^2\rangle, \\ \overline{\alpha}_4 &= \langle k_Q^4\rangle - 3\langle k_Q^2\rangle^2, \\ \overline{\alpha}_6 &= \langle k_Q^6\rangle - 15\langle k_Q^4\rangle\langle k_Q^2\rangle + 30\langle k_Q^2\rangle^3 \end{aligned} \tag{11}$$

are cumulants of $n(s)$. This cumulant expansion contains terms in $n^*(s)$ only, terms arising from atoms above the condensate which contribute at short s in Eqs. (7) and (9). The condensate contribution, which is long range in s, has to be added separately to $n^*(s)$ in Eq. (8) as discussed below. The model $J_{\rm IA}(s)$ has four parameters, n_0, $\overline{\alpha}_2$, $\overline{\alpha}_4$, and $\overline{\alpha}_6$. These are determined as a function of pressure by fitting to experiment in the Results section below.

The model FS function $R(Q,s)$ that we fit to data is obtained by making a cumulant expansion of the intermediate DSF $J(Q,s)$ in Eq. (8). The terms in $J(Q,s) = n^*(s)R(Q,s)$ that belong to $n^*(s)$ [the Q-independent terms in Eq. (10)] are identified and the remaining terms arise from $R(Q,s)$. Up to powers s^6, this gives

$$R(Q,s) = \exp\left[\frac{i\overline{\beta}_3 s^3}{3!} + \frac{\overline{\beta}_4 s^4}{4!} - \frac{i\overline{\beta}_5 s^5}{5!} - \frac{\overline{\beta}_6 s^6}{6!} + \cdots\right]. \tag{12}$$

Expressions for the coefficients $\overline{\beta}_n$ are

$$\begin{aligned} \overline{\beta}_3 &= \overline{a}_3/\lambda Q, \\ \overline{\beta}_4 &= \overline{a}_4/(\lambda Q)^2, \\ \overline{\beta}_5 &= \overline{a}_{52}/(\lambda Q)^3 + \overline{a}_{54}/\lambda Q, \\ \overline{\beta}_6 &= \overline{a}_{62}/(\lambda Q)^4 + \overline{a}_{64}/(\lambda Q)^2, \end{aligned}$$

where the $\overline{a}_{nm}$ are independent of Q and $\lambda = \hbar^2/m = 1.0443$ meV Å^2 in liquid ^{4}He. Expressions for the $\overline{a}_{nm}$ can be derived from the moments of $J(Q,y)$ and expressions up to $\overline{a}_{64}$ have been obtained.[25,39] The lowest two are $\overline{a}_3 = \langle\nabla^2 v(r)\rangle/6$ and $a_4 = \langle(\nabla v)^2\rangle/3$, where $v(r)$ is the total potential seen by the struck atom. In applications[34,40] we have found that $\overline{\beta}_4$ is negligible. Similarly, the $\overline{a}_{54}$ term in $\overline{\beta}_5$ and the $\overline{a}_{62}$ term in $\overline{\beta}_6$ are also small and can be neglected. In this way $R(Q,s)$ reduces to three terms,

$$R(Q,s) = \exp\left\{\frac{i(\overline{a}_3/\lambda Q)s^3}{3!} - \frac{i[\overline{a}_{52}/(\lambda Q)^3]s^5}{5!} - \frac{[\overline{a}_{64}/(\lambda Q)^2]s^6}{6!}\right\}, \tag{13}$$

which depend on three parameters, $\overline{a}_3$, $\overline{a}_{52}$, and $\overline{a}_{64}$. These parameters are determined as a function of pressure by fits of the total $J(Q,y)$ to experiment in the Results section below.

The expressions in Eqs. (10) and (13) were derived for a fluid without a condensate. When there is BEC, we assume that we can replace the $n^*(s)$ in Eq. (10) with $n(s)$ in Eq. (6), which contains the condensate without affecting the short time expansions. This is based on the picture that the condensate term, $n_0[1 + f(s)]$, in $n(s)$ is small and a long-range function in s. As a result, adding it to $n^*(s)$ should not change significantly the expansion of $J(Q,s)$ at short distances s. Empirically, we have found that $R(Q,y)$ is the same within precision above T_λ [where $n(s) = n^*(s)$] and below T_λ [where $n(s) \neq n^*(s)$].

C. Experiment

The data reported here were collected using the MARI time-of-flight (TOF) spectrometer located at the ISIS spallation neutron facility, Rutherford Appleton Laboratory, UK. MARI was chosen because it has a combination of high incident energies (up to 1 eV possible) and a wide and almost continuous angular detector coverage (3 ° to 135 ° in steps of 0.43 °) making it ideal to simultaneously access a large range in energy and momentum transfer. Due to the pulsed nature of the source, data collection is performed in TOF in which the time of arrival of a neutron in the detector, relative to when they leave the moderator, determines its energy loss or gain after scattering from the sample. The momentum transfer depends on the TOF and the scattering angle of the neutron.

Commercial-grade ^{4}He (0.3 ppm of ^{3}He) was condensed in a cylindrical aluminum sample cell of volume 100 cm^3 that is thermally anchored to the mixing chamber of a Vericold dry dilution fridge with a base temperature of 40 mK. Highly neutron absorbing boron nitride (BN) was used as shielding material to reduce undesirable background scattering from the sample cell end caps and exposed parts of the fridge. In addition, to minimizing multiple scattering within the ^{4}He sample, 1-mm-thick BN disks were placed perpendicularly to the cylindrical axis, essentially splitting the sample volume into five smaller cylinders. Temperature was measured using a calibrated RuO2 sensor and the pressure was monitored using a pressure transducer situated in an external gas panel containing a 4-liter buffer volume. The incident neutron energy was determined to be 720 meV.

Data were successfully collected as follows: at base temperature (40 to 75 mK) in the superfluid phase and at pressure, $p = 0$, 7.5, 12, 15, 20, and 24 bar; in the normal phase (2.3 K) and at $p = 12$, 20, and 24 bar; and additionally for $p = 24$ bar at $T = 1.0$, 1.5, and 2.0 K.

The data collected in TOF were then converted to energy transfer ($\hbar\omega$) at constant scattering angle and subsequently to constant scattering vector Q using standard procedures. A detailed discussion of the data transformation from TOF to $S(\phi,\omega)$ and then to $S(Q,\omega)$ is given by Andersen *et al.*[41] As discussed in Sec. II, we expressed the DSF as $J(Q,y) = (\hbar Q/m)S(Q,\omega)$, which is weakly Q dependent as a result of FSE. The experimental data were transformed to $J(Q,y)$ for $Q = 20$ to 29 Å^{-1} in steps of 0.5 Å^{-1} and a sample of the data are shown in From Figs. 1 and 2. Since the observed $J(Q,y)$ consists of a convolution of the underlying momentum distribution, the FS function and the instrumental resolution function, for a quantitative analysis of the data, the instrumental resolution function must be accurately known.

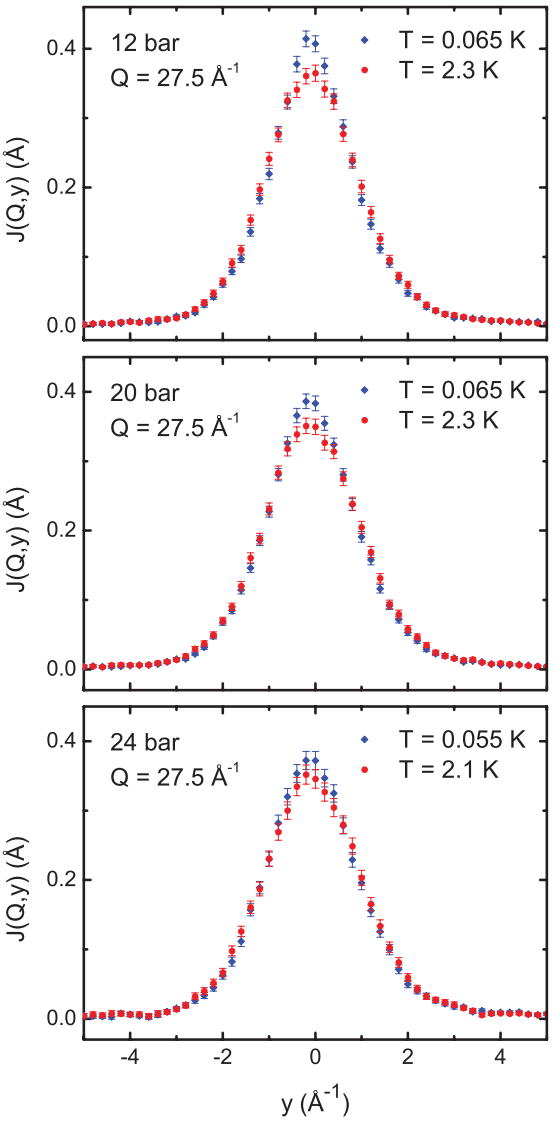

FIG. 1. (Color online) Observed data, the DSF $J(Q,y)$ folded with the instrument resolution, at wave vector $Q = 27.5$ Å^{-1}. Shown is $J(Q,y)$ versus y of liquid ^{4}He at low temperature in the Bose condensed phase (blue diamonds) and in the normal liquid phase (red circles) at three pressures, where $y = (\omega - \omega_R)/v_R$ is the energy transfer, $\omega_R = \hbar\mathbf{Q}^2/2m$, and $v_R = \hbar\mathbf{Q}/m$. The difference between $J(Q,y)$ in the Bose condensed and normal liquid phases decreases with increasing pressure, reflecting a decreasing condensate fraction. (The 12-bar and 24-bar data are from Ref. 38.)

The instrument resolution was calculated using Monte Carlo simulation, as discussed in Ref. 34.

III. RESULTS

A. Data and fits to data

Figure 1 shows the observed DSF, $J(Q,y)$, at constant wave vector $Q = 27.5$ Å^{-1} as a function of y at three pressures. Figure 2 shows similar data at SVP taken from Ref. 34. From Figs. 1 and 2, we see that $J(Q,y)$ at low temperature in the Bose condensed phase has a higher peak at $y \simeq 0$ than $J(Q,y)$ in the normal phase. This reflects the contribution from the condensate, chiefly from the term $n_0R(Q,y)$ in $J(Q,y)$. The

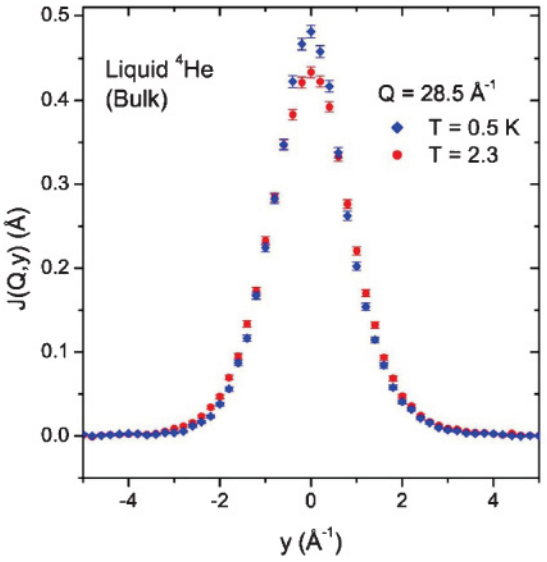

FIG. 2. (Color online) As Fig. 1 for liquid ^{4}He at SVP (from Ref. 34).

width of the additional peak at $y \simeq 0$ at low temperature is set by the width of the FS function $R(Q,y)$. The term $n_0 R(Q,y)$ can also be seen in the data at finite y. The height of the additional peak at low temperature clearly decreases with increasing pressure displaying directly the decrease in condensate fraction with increasing pressure. Figure 3 shows fits to the data at three pressures. Specifically, the model OBDM, given by Eqs. (6) and (10), was multiplied by the FS function $R(Q,s)$ [Eq. (13)] and Fourier transformed as given by Eq. (5) to obtain $J(Q,y)$. The $J(Q,y)$ was convoluted with the MARI instrument resolution function and fitted to the data. The MARI resolution function is shown as a dotted line in Fig. 3. The values of the condensate fraction n_0 that provide the best fit are indicated in Fig. 3. The best values are determined both by the height of the peak at $y \simeq 0$ and by the shape of $J(Q,y)$ in the wings at $y \simeq \pm 2$ Å^{-1}. The sensitivity of the fit to the value of n_0 is displayed in Fig. 4. The best overall fit at all y values is obtained with $n_0 = 3.5\%$. In Fig. 4 we see that the fitted $J(Q,y)$ for $n_0 = 3.5\%$ lies somewhat below the data in the peak region at $y = 0$. This suggests that the FS function is too broad in the peak region, a point we return to in the Discussion. With only three terms, the FS function has a limited flexibility. The four parameters, n_0, $\overline{\alpha}_2$, $\overline{\alpha}_4$, and $\overline{\alpha}_6$ in the OBDM, $n(s)$ in Eqs. (6) and (10), and the three parameters $\overline{a}_3/\lambda$, $\overline{a}_{52}/\lambda^3$, and $\overline{a}_{64}/\lambda^2$ in the FS function $R(Q,s)$ in Eq. (13) were all determined by fits to the data. Specifically, the parameters were determined as those which provided a best overall fit to the data at each Q value at each pressure. Typically, three to four parameters could be determined in a single fit at a given Q and pressure. The parameters as defined above should all be independent of Q. The actual Q dependence of n_0 and $\overline{\alpha}_2$ emerging from the fits is shown in Figs. 5 and 6. There we see that the parameters providing the best fit fluctuate with Q reflecting the statistical nature of the data but are independent of Q. There was clearly correlation between the values of $\overline{\alpha}_2$ and n_0 in $n(s)$ obtained at a given Q. This can be seen in the

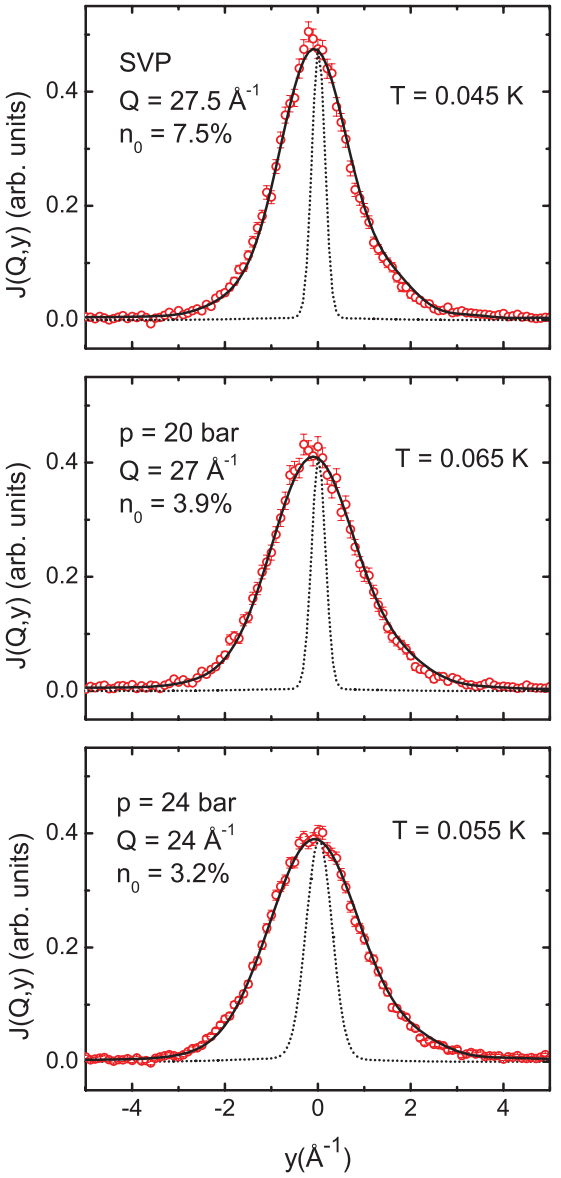

FIG. 3. (Color online) Observed $J(Q,y)$ (open circles) at low temperature showing fits (solid lines) of the model $J(Q,y)$ given by Eqs. (5), (6), (7), and (13) to the data. Both the observed and the fitted $J(Q,y)$ include the MARI instrument resolution function shown by the dotted line. The condensate fraction, n_0, in the model that provides the best fit clearly decreases with increasing pressure.

parameters shown in Figs. 5 and 6 at 20 bar. However, we found that the parameters of $n^*(s)$ and $R(Q,s)$ were reasonably independent. By using parameter values averaged over Q and iterating between the determination of the parameters in $n(s)$ and $R(Q,s)$, we were able to determine all seven parameters with reasonable precision. The values of n_0, $\overline{\alpha}_2$, and $\overline{a}_3/\lambda$ were best determined and the values of $\overline{\alpha}_6$ and $\overline{a}_{64}/\lambda^2$ least well determined. The values of the parameters n_0, $\overline{\alpha}_2$, $\overline{\alpha}_4$, and $\overline{\alpha}_6$ in the momentum distribution determined by a best fit to data are listed in Table I. A condensate fraction of 7% at SVP is obtained from the present data. This agrees within error with our previous value[34] of 7.25%. The n_0 decreases from 7% at SVP to 3.2% at 24 bar.

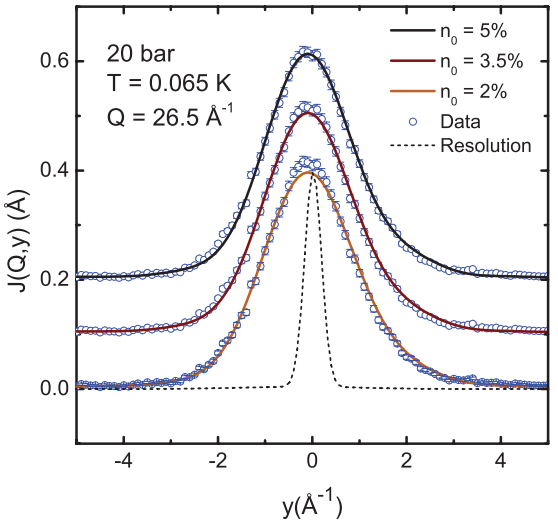

FIG. 4. (Color online) Observed $J(Q,y)$ (open circles) at $T = 0.065$ K and $p = 20$ bar showing fits to data with a preset condensate fraction. The best least squares fit is $n_0 = 3.5\%$. Note that when n_0 is set at 5% the fit is good in the peak region but not good at $y \simeq \pm 2$ Å^{-1}, where the $n_0 R(Q,y)$ term is still important.

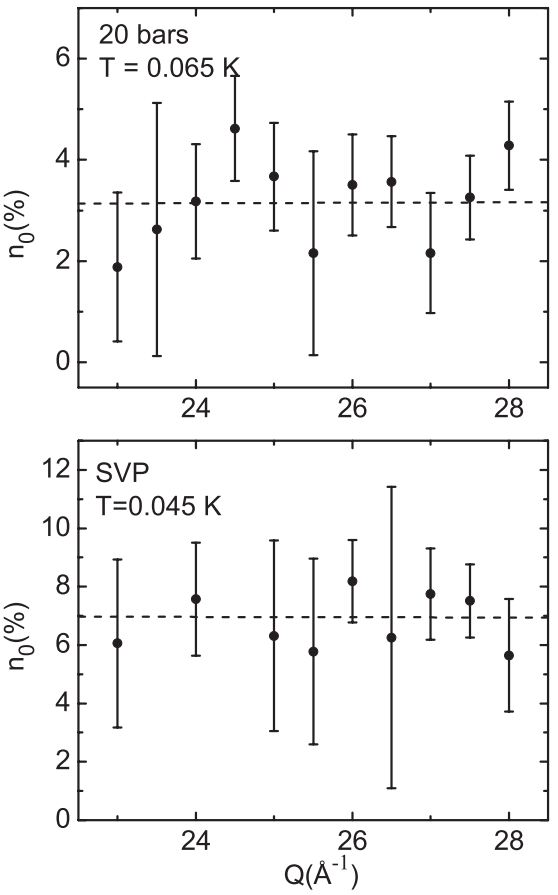

FIG. 5. Condensate fraction, n_0, obtained from fits of Eq. (6) to data at several wave vectors, 23 Å $\leqslant Q \leqslant$ 28Å, and pressures SVP and 20 bar. The best fit n_0 fluctuates from Q to Q, reflecting the statistical error of the data, but n_0 is independent of Q.

Figure 7 shows the parameters $\overline{\alpha}_2$, $\overline{\alpha}_4$, and $\overline{\alpha}_6$ of the OBDM that are listed in Table I as a function of pressure. We note first that the $\overline{\alpha}_2$ parameter, which sets the width of the Gaussian component of the OBDM and of $n^*(\mathbf{k})$, decreases with temperature. The $\overline{\alpha}_2$ and the width of the momentum distribution $n^*(\mathbf{k})$ is larger at high temperature in the normal liquid phase than at low temperature in the Bose condensed phase. This temperature dependence of $\overline{\alpha}_2$ is somewhat unexpected since the temperature is already low and the width is dominated by zero point effects. The drop in $\overline{\alpha}_2$ corresponds to a drop in the atomic kinetic energy of approximately 2.0 K, between $T = 2.3$ K and $T \simeq 0.05$ K, the same as the change in the temperature. We return to this point below. The $\overline{\alpha}_2$ increases with increasing pressure reflecting an increased localization of the atoms and a broadening of the momentum distribution with pressure. The $\overline{\alpha}_4$ parameter also increases with increasing pressure so that the kurtosis of the distribution, $\delta = \overline{\alpha}_4/\overline{\alpha}_2{}^2$, remains approximately independent of pressure at $\delta = 0.40$. Within precision, $\overline{\alpha}_6$ is independent of pressure.

The pressure dependence of the parameters $\overline{a}_3/\lambda$, $\overline{a}_{52}/\lambda^3$, and $\overline{a}_{64}/\lambda^2$ of the FS function are listed in Table II and shown in Fig. 8. All three of the parameters increase with increasing pressure. There is a substantial compensation between the parameters $\overline{a}_3/\lambda$ and $\overline{a}_{52}/\lambda^3$. In fitting the present data, we found best fit values of both $\overline{a}_3/\lambda$ and $\overline{a}_{52}/\lambda^3$ that were larger than those obtained[34] in fits to previous data. For example, the present and previous values of $\overline{a}_3/\lambda$ and $\overline{a}_{52}/\lambda^3$ at SVP are compared in Table II showing that the present values are significantly larger. However, a plot of the two FS functions in Fig. 9 shows that the two FS functions are actually very similar. This is because of the significant compensation between $\overline{a}_3/\lambda$ and $\overline{a}_{52}/\lambda^3$.

B. OBDM, momentum distribution, and condensate fraction

The function, $n(s)$, representing the OBDM that we have fitted to the data is given by Eqs. (6) and (10). The parameters in $n(s)$ obtained from the fits to data are listed in Table I and shown in Fig. 7. The part of the OBDM that represents the fluid above the condensate, $n^*(s)$, given by Eq. (10), is shown in the top panel of Fig. 10 at SVP and 24 bar. The $n^*(s)$ which is short range in s is clearly narrower at 24 bar than at SVP. The narrowing arises from the increased localization of the atoms in space as they are compressed to higher density. The increased localization at higher density is induced by the hard core component of the interatomic potential. The bottom panel of Fig. 10 shows the corresponding momentum distribution, $n^*(\mathbf{k})$, which is broader at 24 bar than at SVP. Since $n^*(\mathbf{k})$ is normalized to unity, the broader $n^*(\mathbf{k})$ at 24 bar must also be smaller at $k = 0$ to preserve normalization.

The full OBDM, given by Eqs. (6), which include the condensate component, $n_0[1 + f(s)]$, is shown in Fig. 5 of Ref. 38. For $s \gtrsim 3.0$ Å, the $n^*(s)$ is effectively zero and $n(s)$ reduces to the long-range component given by $n_0[1 + f(s)]$. The magnitude of the long-range component is set by the condensate fraction n_0. The reader is referred to Ref. 38 for further discussion of the OBDM.

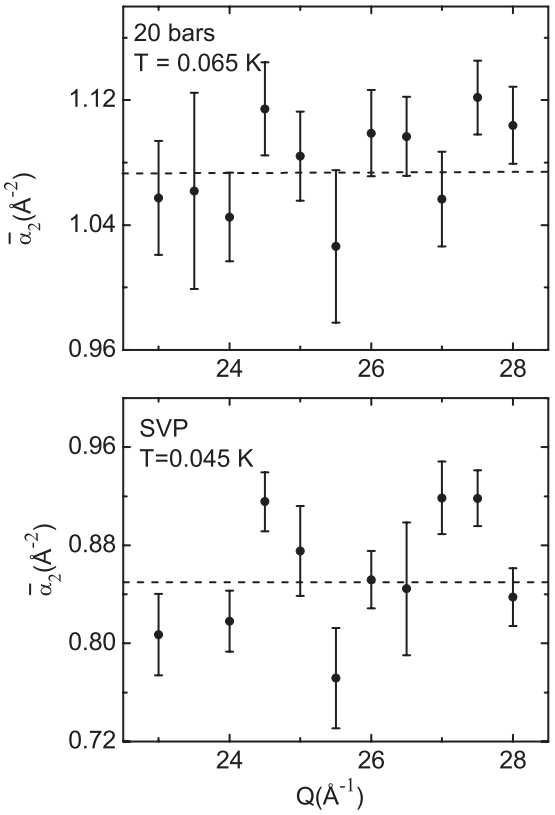

FIG. 6. The parameter $\bar{\alpha}_2 = \langle k_Q^2 \rangle$, which sets the width of the Gaussian component of the OBDM in Eq. (10) obtained from fits to data at several wave vectors, 23 Å $\leqslant Q \leqslant$ 28 Å , and pressures SVP and 20 bar. The $\bar{\alpha}_2$ fluctuates from Q to Q but is independent of Q.

The condensate fraction extracted from the OBDM is shown in Fig. 11. The n_0 decreases from 7.25% ± 0.75% at SVP to 3.2% ± 0.75% at 24 bar. At the liquid/solid boundary, $p =$ 25.3 bar, $n_0 \simeq 3.0\%$. The increased localization of the atoms in space at higher density means that a smaller fraction can be localized in a single state in k space. In Fig. 11 we see that the diffusion Monte Carlo (DMC) values of Moroni and Boninsegni[42] and the path integral ground state (PIGS) values of Rota and Boronat[43] agree well with our observed value. Taken together, the present observed and calculated n_0 provide a reliable value of the condensate fraction at low temperature in liquid ^{4}He as a function of pressure. In the top panel of Fig. 12, we compare the full momentum distribution with its Gaussian component which is obtained by setting the terms in s^4 and s^6 equal to zero in Eq. (10). The full $n^*(\mathbf{k})$ has larger occupation of low momentum states than a Gaussian. The OBDM $n^*(s)$ obtained from the present data at SVP is compared with that determined at SVP in Ref. 34 in the bottom panel of Fig. 12. The agreement is very good with some difference at large s.

C. Final-state function

The FS functions at SVP and at 24 bars are compared in Fig. 13. There we see that $R(Q,s)$ is a smoothly varying function of s and goes uniformly from 1.0 at $s = 0$ to zero at approximately $s = 4$ Å. In the absence of FS effects $R(Q,s) =$ 1 at all s. The FS function in $J(Q,s) = J_{\rm IA}(s)R(Q,s)$ serves to cut off the IA at a finite s value so that $J_{\rm IA}(s)$ can no longer be observed in $J(Q,s)$. Particularly, this means that the condensate fraction in $J_{\rm IA}(s)$ can be observed out to $s \simeq 4$ Å only. This limits the accuracy to which n_0 in $J_{\rm IA}(s)$ can be determined. In contrast the $R(Q,y)$ is an oscillating function of y and apparently very complicated. The representation in y shows that $R(Q,y)$ has a broad peak at $y = 0$. In the absence of FS effects when $R(Q,s) = 1$, the peak is a δ function, $R(Q,y) = \delta(y)$. The peak is broad if $R(Q,s)$ goes to zero at a small value of s. The peak is broader at $p = 24$ bar than at SVP. Finally, the present $R(Q,s)$ at SVP is compared with that obtained from previous data at SVP in Fig. 9. There is some difference arising chiefly from the different values of the parameters $\bar{a}_3/\lambda$ and $\bar{a}_{52}/\lambda^3$ obtained in the two cases.

D. Atomic kinetic energy

The kinetic energy per atom, $\langle K \rangle$, of liquid and solid helium has been extensively investigated.[37,45] It is a fundamental property since it forms part of the total energy, $E = \langle K \rangle + \langle V \rangle$. The atomic kinetic energy reflects the degree of quantumness of the system, of confinement of the atoms in space by their neighbors and the interatomic correlations. In a classical system, $\langle K \rangle = (3/2)k_B T$, an energy of $(1/2)\ k_B T$ for each

TABLE I. Parameters in the OBDM, $J_{\rm IA}(s) = n(s)$, given by Eqs. (6) and (10). The atomic momentum distribution is the 3D Fourier transform of $n(s)$. The parameters are determined by fitting the total DSF $J(Q,y)$ given by Eq. (5) to data as shown, for example, in Fig. 3. The SVP* values are from Ref (34).

P (bar)	T (K)	$\bar{\alpha}_2$ (Å^{-2})	$\bar{\alpha}_4$ (Å^{-4})	$\bar{\alpha}_6$ (Å^{-6})	n_0 (%)
24	0.055	1.10 ± 0.02	0.49 ± 0.10	0.30 ± 0.20	3.2 ± 0.75
24	2.10	1.18 ± 0.02	0.51 ± 0.10	0.30 ± 0.25	
20	0.065	1.08 ± 0.02	0.51 ± 0.10	0.25 ± 0.20	3.5 ± 0.75
20	2.30	1.15 ± 0.02	0.56 ± 0.10	0.38 ± 0.20	
15	0.065	1.05 ± 0.02	0.49 ± 0.10	0.25 ± 0.20	4.4 ± 0.75
12	0.065	1.00 ± 0.02	0.42 ± 0.10	0.30 ± 0.20	4.4 ± 1.00
12	2.30	1.08 ± 0.02	0.52 ± 0.10	0.39 ± 0.30	
7.5	0.075	0.93 ± 0.02	0.39 ± 0.12	0.32 ± 0.20	5.2 ± 1.00
SVP	0.045	0.85 ± 0.02	0.28 ± 0.05	0.38 ± 0.05	7.0 ± 0.75
SVP*	0.5	0.897 ± 0.02	0.46 ± 0.05	0.38 ± 0.04	7.25 ± 0.75

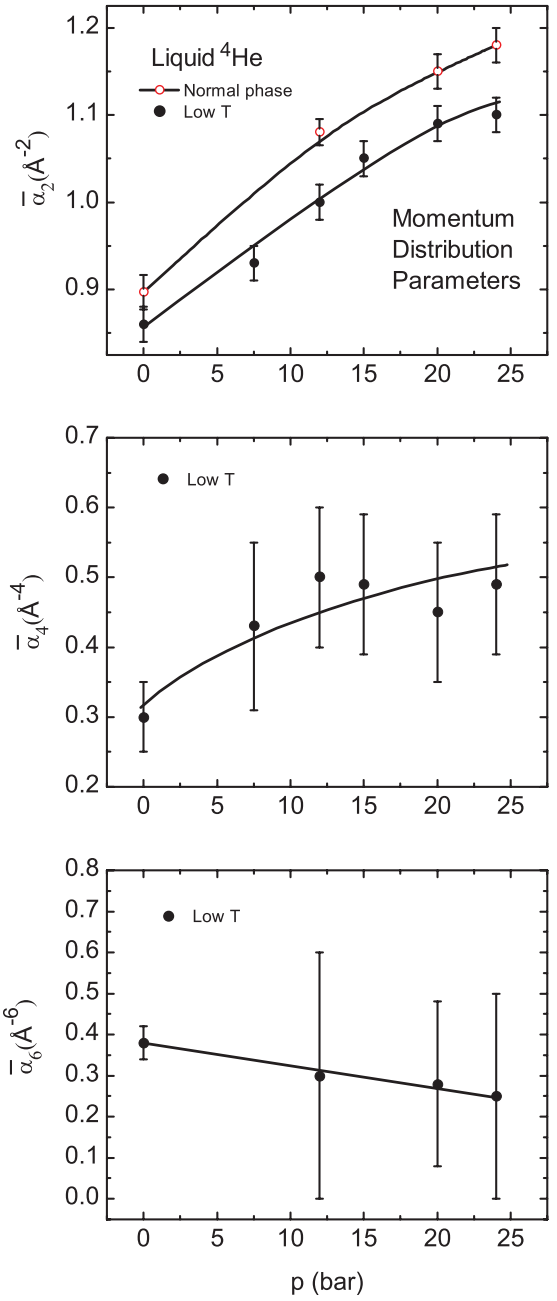

FIG. 7. (Color online) Parameters $\overline{\alpha}_2$, $\overline{\alpha}_4$, and $\overline{\alpha}_6$ that describe the OBDM of the liquid above the condensate, $n^*(s)$, given by Eq. (10), as obtained from fits to the present data. The atomic momentum distribution $n^*(\mathbf{k})$ is the Fourier transform of $n^*(s)$. The $\overline{\alpha}_2$ that determines the Gaussian component of $n^*(s)$ and $n^*(\mathbf{k})$ is larger in the normal liquid phase than in the Bose condensed phase. The $\overline{\alpha}_4$ and $\overline{\alpha}_6$ are independent of temperature within precision.

translational degree of freedom of the atom. In a quantum system, the momentum and position of atoms are coupled. If the atoms are confined in space the $\langle K\rangle$ must increase. The $\langle K\rangle$ can decrease somewhat if the atomic motion is highly correlated in space. A higher correlation means the wave function can be broader and the width in momentum space and $\langle K\rangle$ can be smaller.

Ceperley *et al.*[45] have determined $\langle K\rangle$ in the liquid and solid ^{4}He over a wide range of density and temperature,

TABLE II. Parameters in the FS function $R(Q,s)$ given by Eq. (13) obtained by fitting the total DSF $J(Q,y)$ given by Eq. (5) to data. An example of $R(Q,s)$ is shown in Fig. 13. The SVP* values are from Ref. (34) ($\lambda = \hbar^2/m = 1.0443$ meV Å$^{-1} = 12.12$ K Å^{-1}).

P (bar)	$(\bar{a_3}/\lambda)$ (Å^{-4})	$(\bar{a_{52}}/\lambda^3)$ (Å^{-8})	$(\bar{a_{64}}/\lambda^2)$ (Å^{-8})
24	8.5 ± 0.8	9500 ± 2000	400 ± 200
20	8.0 ± 0.8	8000 ± 800	400 ± 100
15	7.6 ± 1.0	8500 ± 2000	400 ± 150
12	7.4 ± 1.2	7800 ± 1500	240 ± 150
7.5	5.5 ± 0.5	5000 ± 600	180 ± 70
SVP	5.3 ± 0.5	4400 ± 600	170 ± 60
SVP*	2.43 ± 0.25	2560 ± 300	215 ± 25

chiefly at higher temperature, $T \geqslant 5$ K. At lower temperature the $\langle K\rangle$ in the solid depends almost entirely on the solid density and little on the temperature. This reflects the highly quantum nature of the solid (zero point energy dominates the thermal energy) and that phonon energies change little with temperature. In contrast, the $\langle K\rangle$ in the liquid increases with increasing temperature.[45,46] At low temperature, below 2.3 K, it increases because the condensate fraction is decreasing and because the phonon-roton mode energies are decreasing with increasing temperature. Between 2.3 K and 5 K it increases less rapidly but increases rapidly again at higher temperature.

Ceperley *et al.*[45] find that the $\langle K\rangle$ is somewhat lower in the solid than in the liquid at the same density. This indicates that the atomic motion is somewhat more correlated in the solid than in the liquid. The difference increases with increasing temperature since the $\langle K\rangle$ in the liquid increases with temperature. The extensive literature on the $\langle K\rangle$ at temperatures of 4 K and above is reviewed by Andreani *et al.*[37]

The $\langle K\rangle$ in liquid ^{4}He at $T = 0$ K as a function of density has been accurately calculated using Green's function Monte Carlo[47] (GFMC) and DMC[48] methods. At SVP, the temperature dependence of the $\langle K\rangle$ between 1.18 K and 3.33 K has been accurately calculated by path integral Monte Carlo[46] (PIMC). We can determine the $\langle K\rangle$ in this temperature and density range for comparison from our measured momentum distribution as

$$\langle K\rangle = \left(\frac{\hbar^2}{2m}\right)\int d\mathbf{k} n(\mathbf{k})\mathbf{k}^2. \tag{14}$$

Inserting the $n(\mathbf{k})$ given by Eq. (1), we find that the condensate term makes a negligible contribution with all the $\langle K\rangle$ arising from the $n^*(\mathbf{k})$ term. At low temperature in the Bose condensed phase, the resulting $\langle K\rangle$ is

$$\langle K\rangle = \frac{3\hbar^2}{2m} A_1 \overline{\alpha}_2. \tag{15}$$

The constant A_1 is determined by requiring that $n(\mathbf{k})$ be normalized to unity. This normalization requires $n(s=0) = n_0[1 + f(s=0)] + A_1 = 1$. With $f(s=0) = 0.28$, we have $A_1 = 1 - 1.28 n_0$. Using the low-temperature values of $\overline{\alpha}_2$ and n_0 in Table I, we obtain the $\langle K\rangle$ at $T \simeq 0.5$ K listed in Table III.

In the normal phase, where n_0 is zero and $A_1 = 1$, Eq. (15) reduces to $\langle K\rangle = (3\hbar^2/2m)\,\overline{\alpha}_2$. The values of the $\langle K\rangle$ in the normal phase at $T \simeq 2.3$ K, using the $\overline{\alpha}_2$ values in Table I, are

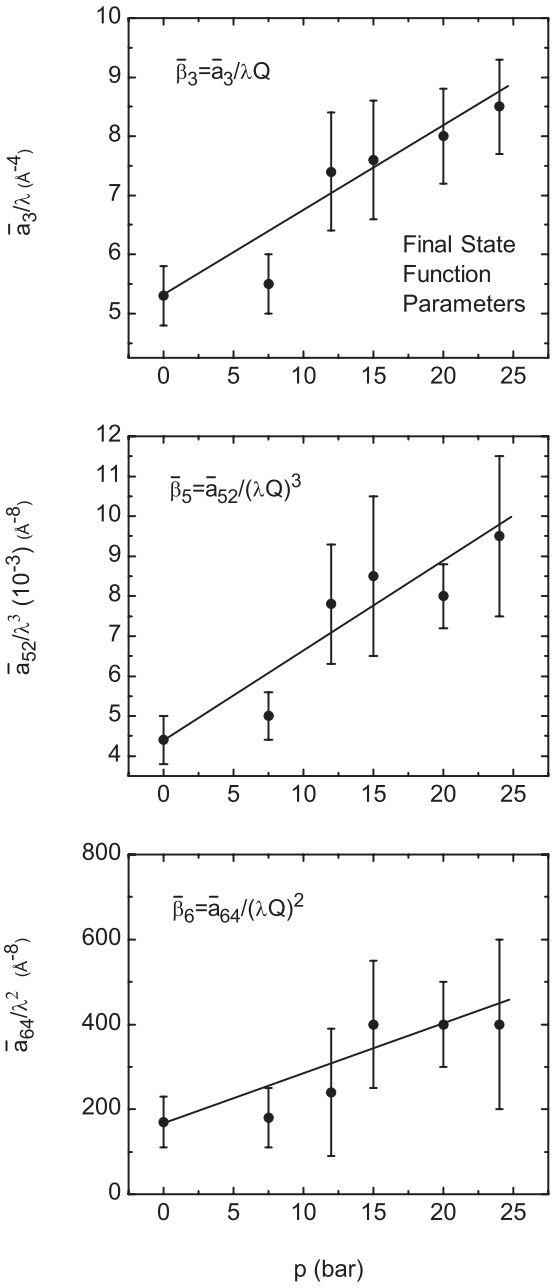

FIG. 8. Parameters that describe the FS broadening function, $R(Q,s)$, given by Eq. (13) and its Fourier transform, $R(Q,y)$, as a function of pressure.

listed in Table IV. The $\langle K\rangle$ values are shown as a function of pressure in Fig. 14.

Figure 15 shows the present $\langle K\rangle$ as a function of density. There we see that the GFMC and DMC values[47,48] of the $\langle K\rangle$ at $T = 0$ K agree well with the present low temperature values. The PIMC values at SVP ($\rho = 0.1451$ g/cm^3) agree well with the present and previous[34] values at SVP. This agreement serves to confirm both the experiment and MC results, since today MC values are very reliable. The $\langle K\rangle$ increases with increasing density as the atoms become more localized in space by their neighbors at higher density. Also shown are $\langle K\rangle$ at 4.25 K observed by Herwig *et al.*[49] and calculated

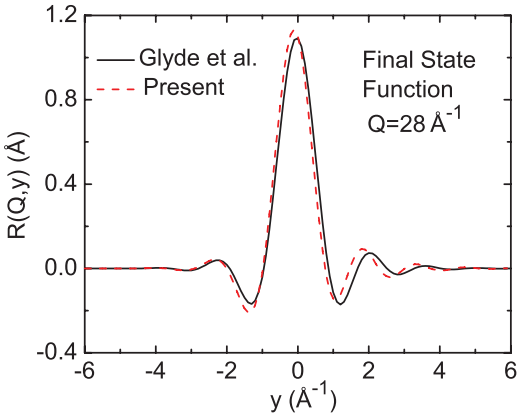

FIG. 9. (Color online) Comparison of the present and previous (Ref. 34) determinations of the FS function $R(Q,y)$ at SVP.

by Ceperley and Pollock.[55] The $\langle K\rangle$ clearly increases with increasing temperature.

Figure 16 shows the present $\langle K\rangle$ values in the liquid compared with those in the solid. The line through the solid $\langle K\rangle$ is simply a best-fit straight line through all the points, observed and calculated. The line through the low-temperature liquid data is a quadratic but a straight line over this short density range fits equally well. The comparison of the solid $\langle K\rangle$ and the liquid $\langle K\rangle$ at low temperature in Fig. 16 confirms, within error, that the $\langle K\rangle$ of the two differ little at the liquid/solid boundary at low temperature, as demonstrated

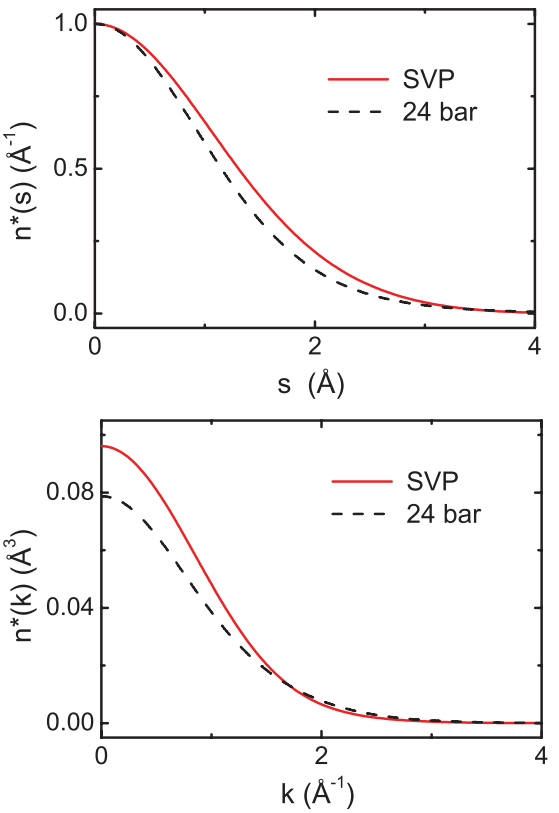

FIG. 10. (Color online) The OBDM, $n^*(s)$, given by Eq. (8) and its Fourier transform the 3D momentum distribution, $n^*(\mathbf{k})$, for the liquid above the condensate at SVP and 24 bar.

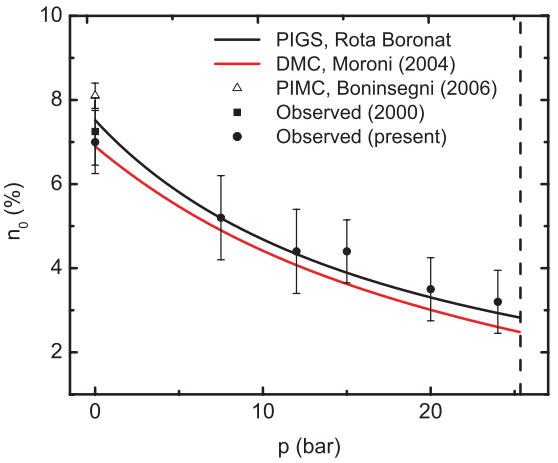

.

FIG. 11. (Color online) Condensate fraction, n_0, at low temperature ($T \leqslant 0.075$ K) in liquid ^{4}He versus pressure (solid circles) obtained from fits to the present data. Also shown are PIGS values calculated by Rota and Boronat (Ref. 43) and DMC values by Moroni and Boninsegni (Ref. 42) (Moroni 2004). At SVP, values calculated by Boninsegni *et al*. (Ref. 44) (open triangle) and observed previously (Ref. 34) (solid square) are also shown (from Ref. 38).

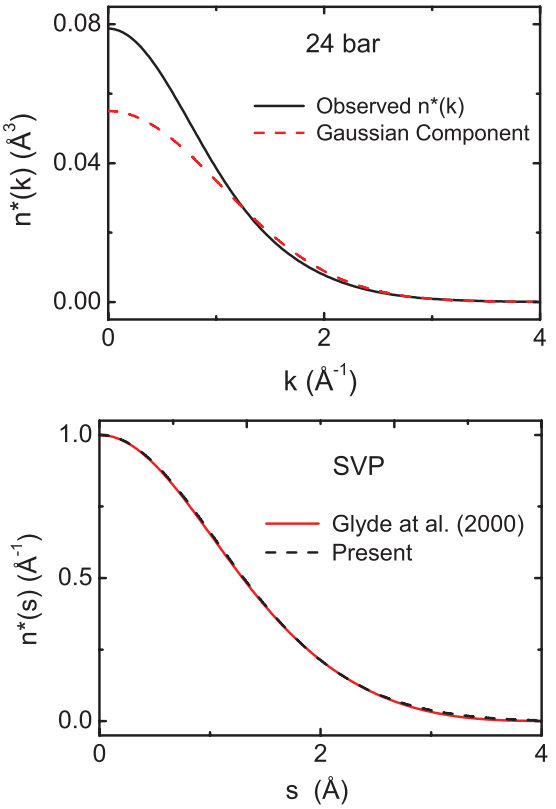

FIG. 12. (Color online) The full $n^*(\mathbf{k})$ has larger occupation of low-momentum states than a Gaussian. The OBDM $n^*(s)$ obtained from the present data at SVP is compared with that determined at SVP in Ref. 34. The agreement is very good with some difference at large s.

previously by Ceperley *et al*.[45] At higher temperature the $\langle K\rangle$ in the liquid is higher than that in the solid at the boundary, since the liquid $\langle K\rangle$ increases with temperature while that in the solid is approximately independent of temperature, again as shown previously.[45]

IV. DISCUSSION

A. Condensate fraction

In the present measurements, we find a condensate fraction that decreases with increasing pressure from from $n_0 = 7.25\% \pm 0.75\%$ at SVP ($p \simeq 0$) to $n_0 = 3.2\% \pm 0.75\%$ at pressure $p = 24$ bar. These values are significantly less than those found initially in the pioneering measurements of Snow *et al*.[31] The pressure dependence is also different. The n_0 of Snow *et al*. are compared with the present n_0 in Fig. 6 of Ref. 38.

The condensate fraction can also be obtained from the difference in kinetic energy of the liquid in the normal and superfluid phases, a method proposed by Sears.[56] The central assumption is that the difference between $\langle K\rangle$ above and below T_λ arises solely from BEC. The expression for n_0 can be obtained from Eq. (15). Specifically, the $\langle K\rangle$ in the normal phase is $\langle K\rangle_N = \frac{3\hbar^2}{2m}\overline{\alpha}_2(N)$, where $\overline{\alpha}_2(N)$ is the second moment of $n^*(\mathbf{k})$, the atomic momentum distribution of the atoms above the condensate in Eq. (1), in the normal phase. In contrast, at $T \simeq$, 0 where there is BEC, the $\langle K\rangle$ is $\langle K\rangle_0 = \frac{3\hbar^2}{2m}A_1\overline{\alpha}_2(0)$, where $\overline{\alpha}_2(0)$ is the second moment of $n^*(\mathbf{k})$ in the superfluid phase at $T \simeq 0$ and $A_1 = 1 - f(s=0)n_0$. If we assume the $\overline{\alpha}_2$ does not change with temperature $[\overline{\alpha}_2(0) = \overline{\alpha}_2(N)]$, then n_0 is obtained from the $\langle K\rangle$ as $n_0 = [1 - \langle K\rangle_0/\langle K\rangle_N]/f(s=0)$, where $f(s=0) = 1.28$. The $\langle K\rangle_N$ and $\langle K\rangle_0$ are determined experimentally from the second moment of $J_{\rm IA}(y)$ above and below T_λ. Using this method, in two separate measurements[57,58] of $\langle K\rangle$, Mayers *et al*. find $n_0 = 15\% \pm 4\%$ and $n_0 = 8.8\% \pm 0.3\%$ at SVP.

The n_0 determined from the $\langle K\rangle$ are generally larger than those determined by fits of the same model $n(\mathbf{k})$ to data. This is because part of the decrease in $\langle K\rangle$ below T_λ arises from a decrease in $\overline{\alpha}_2$. Assuming $\overline{\alpha}_2$ is constant and that all the change in $\langle K\rangle$ arises from BEC leads to an overestimate of n_0. To illustrate this effect we use the present values of $\overline{\alpha}_2$ and $\langle K\rangle$. The difference between $\overline{\alpha}_2$ in the normal phase and at low temperature is shown in Table I and Fig. 7. Using the kinetic energies in Tables III and IV, $\langle K\rangle_N = 16.3 \pm 0.3$ K and $\langle K\rangle_0 = 14.25 \pm 0.3$ K at SVP and the expression in the paragraph above, we obtain $n_0 = 9.8\% \simeq 10\%$. We may correct this $n_0$value for the change in $\overline{\alpha}_2$ by estimating the change in $\langle K\rangle$ arising from $\overline{\alpha}_2$ alone. This is $\delta\langle K\rangle = \langle K\rangle_N - \langle K\rangle_0 = \langle K\rangle_N[1 - \overline{\alpha}_2(0)/\overline{\alpha}_2(\mathrm{N})] \simeq 0.041\langle K\rangle_N \simeq 0.67$ K. Thus, approximately 30% of the drop in $\langle K\rangle$ below T_λ arises from $\overline{\alpha}_2$ so that n_0 is overestimated by approximately 30%. The corrected n_0 is $n_0 \simeq 7\%$, in agreement with present value obtained by fitting $n(\mathbf{k})$ in Eq. (1) to data at SVP. The relative correction for the change in $\overline{\alpha}_2$ will be much larger at higher pressure where n_0 is smaller.

As shown in Fig. 11, the condensate fractions calculated by MC methods agree very well with the present observed values. This confirms the accuracy of the MC calculations, at least over this limited pressure range. Over a wider pressure range, the MC calculations find that n_0 decreases from $n_0 = 28\%$ at

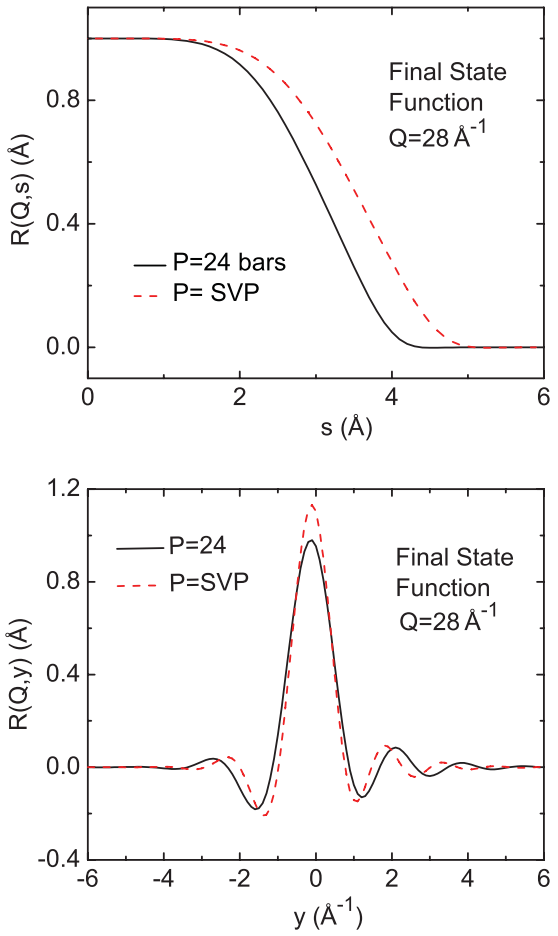

FIG. 13. (Color online) Final-state function $R(Q,s)$ and its Fourier transform $R(Q,y)$ given by Eq. (13) at SVP and at 24 bar. The $R(Q,s)$ goes to zero at smaller values of s and $R(Q,y)$ broadens at higher pressure (lower panel from Ref. 38).

the spinodal density ($\rho = 0.1063$ g/cm^3)($p \simeq -10$ bar)[42] to $n_0 = 0.5\%$ at $p = 300$ bar.[59] At high pressure, the calculated n_0 decreases exponentially with increasing pressure[59] but does not go to zero. Whenever there is BEC, the bulk liquid will have a superfluid density of $\rho_S = 1$ at $T = 0$ K independent of the magnitude of n_0. Thus, bulk liquid ^{4}He is expected to remain superfluid up to high pressures.

TABLE III. The atomic kinetic energy $\langle K\rangle$ of liquid ^{4}He at low temperature. When there is a condensate, $\langle K\rangle = \frac{3\hbar^2}{2m} A_1\ \bar{\alpha}_2$, where $A_1 = 1$–$1.28 n_0$, as discussed in the text ($\hbar^2/m = 1.0443$ meV Å^{-1} = 12.12 K Å^{-1}).

P (bar)	T (K)	n_0 (%)	A_1	$\bar{\alpha}_2$ (Å^{-2})	$\langle K\rangle$ (K)
SVP	0.045	7.0 ± 0.75	0.910	0.86 ± 0.02	14.25 ± 0.3
7.5	0.075	5.2 ± 1.0	0.933	0.93 ± 0.03	15.8 ± 0.4
12	0.065	4.4 ± 1.0	0.944	1.00 ± 0.02	17.2 ± 0.4
15	0.065	4.4 ± 0.75	0.944	1.05 ± 0.02	18.1 ± 0.3
20	0.065	3.5 ± 0.75	0.955	1.08 ± 0.02	18.75 ± 0.3
24	0.055	3.2 ± 0.75	0.959	1.10 ± 0.02	19.2 ± 0.3

TABLE IV. The atomic kinetic energy $\langle K\rangle$ in normal liquid ^{4}He at the temperatures indicated ($\hbar^2/m = 1.0443$ meV Å^{-1}= 12.12 K Å^{-1}).

P (bar)	T (K)	$\bar{\alpha}_2$ (Å^{-2})	$\langle K\rangle$ (K)
SVP*	2.3	0.897 ± 0.02	16.3 ± 0.3
12	2.3	1.08 ± 0.02	19.6 ± 0.3
20	2.3	1.15 ± 0.02	20.9 ± 0.3
24	2.1	1.18 ± 0.02	21.45 ± 0.3

In equilibrium, bulk liquid ^{4}He solidifies to a crystalline solid at 25.3 bar. MC calculations predict a negligible condensate fraction in perfect crystalline solid helium.[60–62] If, however, the solid is held in an amorphous rather than a crystalline structure in simulations, then a condensate fraction of $n_0 \simeq 0.5\%$ is predicted.[61] A solid containing vacancies is also predicted to have a condensate fraction; for example, $n_0 = 0.09\%$ for a vacancy concentration of $c_V = 0.6\%$ at $p \simeq 40$ bars[63] and $n_0 = 0.23\%$ for a $c_V = 1\%$ at pressure $p = 54$ bars.[64] An amorphous solid is observed[65–67] in porous media if the pore diameter is $d \lesssim 50$ Å. The static structure factor of the amorphous solid differs little from that of the liquid.[65–67] Assuming the liquid and amorphous solid have similar condensate fractions, the values of n_0 observed here suggest that there will be a small but finite $n_0 (n_0 \simeq 0.5\%$–$1.0\%)$ in amorphous solid helium at pressures $p \simeq 40$ bar. A condensate fraction has not been observed in crystalline solid helium[40,68,69] at these pressures, even when the surface area is large.[69] An upper limit of $n_0 \leqslant 0.3\%$ has been set.[69] Observation of a condensate fraction in solid helium would be an unambiguous verification of the reports of possible superflow in solid helium.[70–72]

B. Momentum distribution

To obtain a functional form for the momentum distribution, $n^*(\mathbf{k})$, we made a cumulant expansion of the OBDM in Eq. (10). The leading term in the expansion is a Gaussian

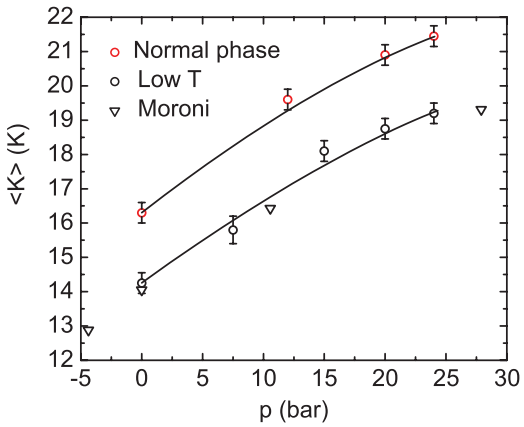

FIG. 14. (Color online) Atomic kinetic energy, $\langle K\rangle$, of liquid ^{4}He versus pressure in the normal phase and at low temperature in the Bose condensed phase. The $\langle K\rangle$ is given by $(3\hbar^2/2m)A_1\bar{\alpha}_2$, where $A_1 = 1 - n_0[1 + f(s=0)]$ and $f(s=0) = 0.28$ and $\hbar^2/m = 12.12$ K Å^2 = 1.0443 meV Å^2. The $T = 0$ K, DMC calculated values of Moroni *et al.* (Ref. 48) are also shown.

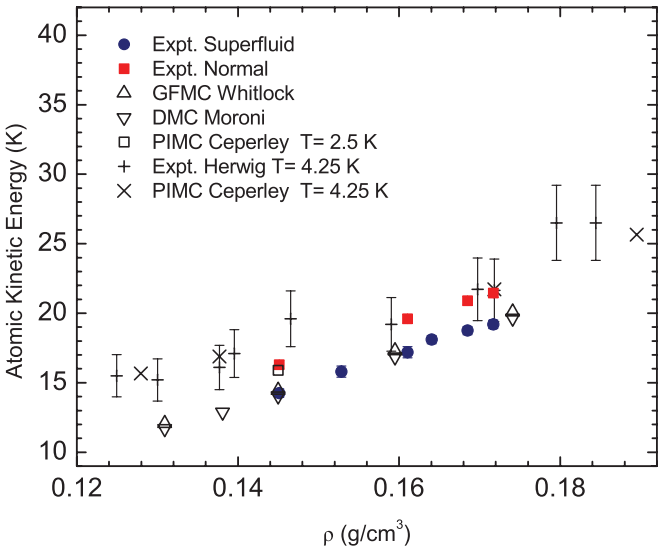

FIG. 15. (Color online) Kinetic energy per atom of liquid ^{4}He versus density. The blue dots ($T = 0.05$ K) and red squares ($T = 2.3$ K) are the present measurements. The open triangles are ground state ($T = 0$ K) calculations of Whitlock and Panoff (Ref. 47) and Moroni *et al*. (Ref. 48). The open square is from Ceperley and Pollock (Ref. 46). The vertical lines with error bars and the crosses are values observed by Herwig *et al*. (Ref. 49) and calculated by Ceperley (Ref. 49), at $T = 4.25$ K, respectively.

of width set by the second cumulant. If the OBDM and its Fourier transform $n^*(\mathbf{k})$ are Gaussian, all higher-order cumulants beyond the Gaussain vanish [i.e., $\overline{\alpha}_4 = \overline{\alpha}_6 = 0$ in Eq. (10)]. We find that the chief effect of pressure is to increase the width of the Gaussian component of $n^*(\mathbf{k})$ [i.e., $\overline{\alpha}_2$ increases with increasing pressure as shown in Fig. (7)]. The increase of width with pressure is reproduced by Monte Carlo calculation.[43] We also note that the width increases with temperature. Specifically, the width, $\overline{\alpha}_2$, of $n^*(\mathbf{k})$ is larger in the normal phase than at low temperature. This means that the observed decrease in $\langle K \rangle$ with decreasing temperature below T_c arises from both BEC and a reduction in width of the intrinsic $n^*(\mathbf{k})$. As a result determinations of the condensate fraction from the T dependence of $\langle K \rangle$ with the assumption that $n^*(\mathbf{k})$ is independent of T will overestimate n_0.

In previous measurements[34,49] of $n^*(\mathbf{k})$ in liquid ^{4}He, non-Gaussian atomic momentum distributions have been observed. In the present and earlier treatments,[34] the deviation from a Gaussian is characterized by the magnitude of the higher-order cumulants [i.e., of $\overline{\alpha}_4$ and $\overline{\alpha}_6$ in Eq. (10)]. The leading deviation from a Gaussian is given by the kurtosis, $\delta = \overline{\alpha}_4/\overline{\alpha}_2{}^2$. In the present measurements, we find $\delta = 0.4$ independent of pressure within present error, the same as found[34] previously at SVP. In liquid neon a smaller value of δ was observed.[36] Calculations[46] of the shape of $n(\mathbf{k})$ in liquid ^{4}He at SVP agreed well[34] with the observed $n(\mathbf{k})$.

If the higher-order cumulants are not large, the exponential in Eq. (10) can be expanded as

$$J^*_{\mathrm{IA}}(s) = n^*(s) = \exp\left(-\frac{\overline{\alpha}_2 s^2}{2!}\right)\left[1 + \frac{\overline{\alpha}_4 s^4}{4!} - \frac{\overline{\alpha}_6 s^6}{6!}\right]. \tag{16}$$

Keeping only the fourth-order term in this OBDM, the corresponding 3D momentum distribution, the Fourier transform of the OBDM $n^*(\mathbf{r})$, is

$$n(\mathbf{k}) = \frac{1}{(2\pi\overline{\alpha}_2)^{3/2}} \exp\left(-\frac{k^2}{2\overline{\alpha}_2}\right) \times \left[1 + \frac{\delta}{8}\left(5 - \frac{10k^2}{3\overline{\alpha}_2} + \frac{k^4}{3\overline{\alpha}_2^2}\right)\right]. \tag{17}$$

This expression, the current values of $\overline{\alpha}_2$ in Table I, and $\delta = 0.4$ provide a reasonably accurate representation of $n(\mathbf{k})$ in liquid ^{4}He as a function of pressure. Measurements at higher-momentum transfer at SVP are consistent[37] with this expression for $n(\mathbf{k})$.

C. Final-state function

The FS function $R(Q,y)$ is the Fourier transform of the intermediate FS function $R(Q,s)$. The intermediate FS function, $R(Q,s)$, that we have used in the intermediate DSF, $J(Q,s) = J_{\mathrm{IA}}(s)R(Q,s)$, is given by Eq. (13). The functional form of $R(Q,s)$ is obtained by expanding $J(Q,s)$ in powers of s as discussed above Eq. (12) and retaining terms up to s^6. Thus, $R(Q,s)$ is valid at short s (at high Q) up to powers of s^6. Since the leading term in $R(Q,s)$ is s^3, $R(Q,s)$ has four terms in s. We found the term in s^4 small, so this term was neglected. The $R(Q,s)$ in Eq. (13) that was fitted to data has three terms and depends on three parameters. The parameters in $R(Q,s)$ can be determined from fits to data over a range of Q values because $R(Q,s)$ depends on Q while $J_{\mathrm{IA}}(s)$ does not. The function $R(Q,s)$ in Eq. (13) with the parameters

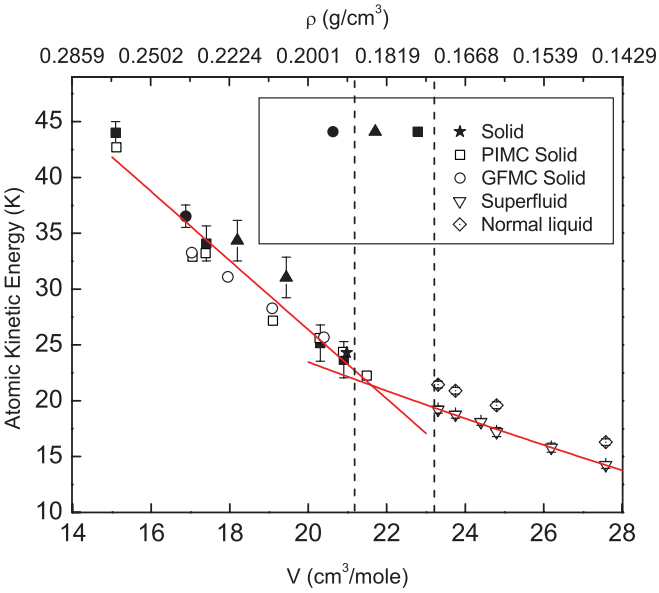

FIG. 16. (Color online) Kinetic energy per atom in solid and liquid ^{4}He. The solid symbols are experimental values in the solid from Hilleke *et al*. (Ref. 50) (solid triangles), Celli *et al*. (Ref. 51) (solid circle), Blasdell *et al*. (Ref. 52) (solid squares), and Diallo *et al*. (Ref. 53) (solid star). The open circles and squares are calculations in the solid from Whitlock and Panoff (Ref. 47) and from Ceperley Refs. 52 and 54. The open triangles and diamonds are the present measurements in the liquid.

in Table II provide a FS function that can be used over a range wave vectors 15 $Å^{-1} \leqslant Q \leqslant 40$ $Å^{-1}$ and temperatures $0 \leqslant T \leqslant 3$ K. Within precision, we found that $R(Q,y)$ was independent of T up to 3 K. The $R(Q,s)$ in Eq. (13) probably provides a reasonable estimate up to 100 $Å^{-1}$.

The chief limitation of the present $R(Q,s)$ is that it has only three terms. The $R(Q,s)$ has limited flexibility in fits to data. For example, the $R(Q,y)$ shown in Fig. (3) appears to be too broad in the peak region at $y \simeq 0$. The width of the $J(Q,y)$ at $y \simeq 0$ is largely limited by the width of the FS function and FS function is not sufficiently flexible to assume a narrow peak and also fit well over a wide range of y values. In Ref. 34 a comparison of the present $R(Q,y)$ with calculated $R(Q,y)$ showed that the present $R(Q,y)$ was broader in the peak region than all calculated $R(Q,y)$. At the same time the n_0 extracted from the data using the calculated $R(Q,y)$ was always less than that obtained using Eq. (13). At this time we believe that the determination of the FS function is the weakest part of the data analysis. The FS function could be improved by introducing a model function that captures the physics of the recoil more precisely than an expansion in powers of s.

ACKNOWLEDGMENTS

This work was supported by the DOE, Office of Basic Energy Sciences under Contract No. ER46680. We acknowledge the scientific and technical support of the staff of the ISIS Spallation Neutron Source, especially of the valuable assistance of Richard Down, where these measurements were conducted and the hospitality of the Institut Laue Langevin, where this paper was written.

[1] A. Griffin, D. Snoke, and S. Stringari (editors), *Bose-Einstein Condensation* (Cambridge University Press, Cambridge, 1995).
[2] A. J. Leggett, in *Modern Trends in the Theory of Condensed Matter*, edited by A. A. Pekalski and R. Przystawa (Springer-Verlag, Berlin, 1980).
[3] P. Nozières and S. Schmitt-Rink, J. Low Temp. Phys. **59**, 195 (1985).
[4] M. Randeria, in *Bose Einstein Condensation*, edited by A. Griffin, D. Snoke, and S. Stringari (Cambridge University Press, Cambridge, 1995).
[5] A. J. Leggett, Rev. Mod. Phys. **73**, 307 (2001).
[6] P. Nozières and D. Pines, *Theory of Quantum Liquids* (Addison-Wesley, Redwood City, CA, 1990), Vol. II.
[7] G. Baym, *Mathematical Methods in Solid State and Superfluid Theory* (Oliver and Boyd, Edinburgh, 1969), pp. 121–156.
[8] J. Klaers, J. Schmitt, F. Vewinger, and M. Weitz, Nature (London) **468**, 545 (2010).
[9] P. O. Löwdin, Phys. Rev. **97**, 1474 (1955).
[10] J. L. DuBois and H. R. Glyde, Phys. Rev. A **63**, 023602 (2001).
[11] G. E. Astrakharchik and K. V. Krutitsky, e-print arXiv:1102.3565 (to be published).
[12] M. H. Anderson, J. R. Ensher, M. R. Matthews, C. E. Wieman, and E. A. Cornell, Science **269**, 198 (1995).
[13] K. B. Davis, M. O. Mewes, M. R. Andrews, N. J. van Druten, D. S. Durfee, D. M. Kurn, and W. Ketterle, Phys. Rev. Lett. **75**, 3969 (1995).
[14] C. C. Bradley, C. A. Sackett, J. J. Tollett, and R. G. Hulet, Phys. Rev. Lett. **75**, 1687 (1995); **79**, 1170 (1997).
[15] A. Miller, D. Pines, and P. Nozières, Phys. Rev. **127**, 1452 (1962).
[16] P. C. Hohenberg and P. M. Platzman, Phys. Rev. **152**, 198 (1966).
[17] P. E. Sokol, in *Bose Einstein Condensation*, edited by A. Griffin, D. Snoke, and S. Stringari (Cambridge University Press, Cambridge, 1995), p. 51.
[18] H. R. Glyde, *Excitations in Liquid and Solid Helium* (Oxford University Press, Oxford, 1994).
[19] R. N. Silver and P. E. Sokol, *Momentum Distributions* (Plenum, New York, 1989).
[20] H. R. Glyde and E. C. Svensson, in *Methods of Experimental Physics, Neutron Scattering. Part B. Neutron Scattering in Condensed Matter Research*, edited by D. L. Price and K. Sköld (Academic Press, San Diego, 1987), Vol. 23, Chap. 13, pp. 303–403.
[21] E. C. Svensson and V. F. Sears, *Frontiers of Neutron Scattering*, edited by R. J. Birgeneau, D. E. Moncton, and A. Zilinger (North-Holland, Amsterdam, 1986).
[22] E. C. Svensson, in *Proceedings of the Los Alamos Workshop on Neutron Scattering* (Report No. LA-10227-C, 1984), Vol. 2, p. 456.
[23] P. Martel, E. C. Svensson, A. D. B. Woods, V. F. Sears, and R. A. Cowley, J. Low Temp. Phys. **23**, 285 (1976).
[24] V. F. Sears, E. C. Svensson, P. Martel, and A. D. B. Woods, Phys. Rev. Lett. **49**, 279 (1982).
[25] V. F. Sears, Phys. Rev. B **30**, 44 (1984).
[26] H. A. Mook, Phys. Rev. Lett. **51**, 1454 (1983).
[27] T. R. Sosnick, W. M. Snow, P. E. Sokol, and R. N. Silver, Europhys. Lett. **9**, 707 (1990).
[28] T. R. Sosnick, W. M. Snow, and P. E. Sokol, Phys. Rev. B **41**, 11185 (1990).
[29] T. R. Sosnick, W. M. Snow, R. N. Silver, and P. E. Sokol, Phys. Rev. B **43**, 216 (1991).
[30] W. M. Snow and P. E. Sokol, J. Low Temp. Phys. **80**, 197 (1990).
[31] W. M. Snow, Y. Wang, and P. E. Sokol, Europhys. Lett. **19**, 403 (1992).
[32] H. A. Gersch and L. J. Rodriguez, Phys. Rev. A **8**, 905 (1973).
[33] R. N. Silver, Phys. Rev. B **39**, 4022 (1989).
[34] H. R. Glyde, R. T. Azuah, and W. G. Stirling, Phys. Rev. B **62**, 14337 (2000).
[35] S. O. Diallo, J. V. Pearce, R. T. Azuah, F. Albergamo, and H. R. Glyde, Phys. Rev. B **74**, 144503 (2006).
[36] R. T. Azuah, W. G. Stirling, H. R. Glyde, P. E. Sokol, and S. M. Bennington, Phys. Rev. B **51**, 605 (1995).
[37] C. Andreani, D. Colognesi, J. Mayers, G. F. Reiter, and R. Senesi, Adv. Phys. **54**, 377 (2005).
[38] H. R. Glyde, S. O. Diallo, R. T. Azuah, O. Kirichek, and J. W. Taylor, Phys. Rev. B **83**, 100507 (2011).
[39] H. R. Glyde, Phys. Rev. B **50**, 6726 (1994).
[40] S. O. Diallo, J. V. Pearce, R. T. Azuah, O. Kirichek, J. W. Taylor, and H. R. Glyde, Phys. Rev. Lett. **98**, 205301 (2007).
[41] K. H. Andersen, W. G. Stirling, H. R. Glyde, R. T. Azuah, A. D. Taylor, S. M. Bennington, and Z. A. Bowden, Physica B **197**, 198 (1994).
[42] S. Moroni and M. Boninsegni, J. Low Temp. Phys. **136**, 129 (2004).
[43] R. Rota and J. Boronat (unpublished).

[44]M. Boninsegni, N. V. Prokof'ev, and B. V. Svistunov, Phys. Rev. E **74**, 036701 (2006).
[45]D. M. Ceperley, R. O. Simmons, and R. C. Blasdell, Phys. Rev. Lett. **77**, 115 (1996).
[46]D. M. Ceperley and E. L. Pollock, Can. J. Phys. **65**, 1416 (1987).
[47]P. A. Whitlock and R. M. Panoff, Can. J. Phys. **65**, 1409 (1987).
[48]S. Moroni, S. Fantoni, and G. Senatore, Phys. Rev. B **52**, 13547 (1995).
[49]K. W. Herwig, P. E. Sokol, T. R. Sosnick, W. M. Snow, and R. C. Blasdell, Phys. Rev. B **41**, 103 (1990).
[50]R. O. Hilleke, P. Chaddah, R. O. Simmons, D. L. Price, and S. K. Sinha, Phys. Rev. Lett. **52**, 847 (1984).
[51]M. Celli, M. Zoppi, and J. Mayers, Phys. Rev. B **58**, 242 (1998).
[52]R. C. Blasdell, D. M. Ceperley, and R. O. Simmons, Z. Naturforsch., A: Phys. Sci. **48**, 433 (1993).
[53]S. O. Diallo, J. V. Pearce, R. T. Azuah, and H. R. Glyde, Phys. Rev. Lett. **93**, 075301 (2004).
[54]D. M. Ceperley, Rev. Mod. Phys. **67**, 279 (1995).
[55]D. M. Ceperley and E. L. Pollock, Phys. Rev. Lett. **56**, 351 (1986).
[56]V. F. Sears, Phys. Rev. B **28**, 5109 (1983).
[57]J. Mayers, C. Andreani, D. Colognesi, J. Phys. Condens. Matter **9**, 10639 (1997).
[58]J. Mayers, F. Albergamo, and D. Timms, Physica B **276–278**, 811 (2000).
[59]L. Vranjes, J. Boronat, J. Casulleras, and C. Cazorla, Phys. Rev. Lett. **95**, 145302 (2005).
[60]D. M. Ceperley and B. Bernu, Phys. Rev. Lett. **93**, 155303 (2004).
[61]M. Boninsegni, Nikolay Prokof'ev, and B. V. Svistunov, Phys. Rev. Lett. **96**, 070601 (2006).
[62]B. K. Clark and D. M. Ceperley, Phys. Rev. Lett. **96**, 105302 (2006).
[63]R. Rota and J. Boronat, J. Low Temp. Phys. **162**, 146 (2011).
[64]D. E. Galli and L. Reatto, Phys. Rev. Lett. **96**, 165301 (2006).
[65]J. Bossy, J. V. Pearce, H. Schober, and H. R. Glyde, Phys. Rev. Lett. **101**, 025301 (2008).
[66]J. Bossy, J. V. Pearce, H. Schober, and H. R. Glyde, Phys. Rev. B **78**, 224507 (2008).
[67]J. Bossy, T. Hansen, and H. R. Glyde, Phys. Rev. B **81**, 184507 (2010).
[68]M. A. Adams, J. Mayers, O. Kirichek, and R. B. E. Down, Phys. Rev. Lett. **98**, 085301 (2007).
[69]S. O. Diallo, R. T. Azuah, O. Kirichek, J. W. Taylor, and H. R. Glyde, Phys. Rev. B **80**, 060504 (2009).
[70]E. Kim and M. H. W. Chan, Science **305**, 1941 (2004).
[71]E. Kim and M. H. W. Chan, Nature (London) **427**, 225 (2004).
[72] S. Balibar, Nature (London) **464**, 176 (2010).